Extending Phenomenological Crystal-Field Methods to C_1 Point-Group Symmetry: Characterization of the Optically Excited Hyperfine Structure of $^{167}Er^{3+}:Y_2SiO_5$

S. P. Horvath,[1,2,3,*] J. V. Rakonjac,[2,3] Y.-H. Chen,[2,3] J. J. Longdell,[2,3] P. Goldner,[4] J.-P. R. Wells,[1,3] and M. F. Reid[1,3,†]
[1]School of Physical and Chemical Sciences, University of Canterbury, PB 4800, Christchurch 8140, New Zealand
[2]Department of Physics, University of Otago, PB 56, Dunedin 9016, New Zealand
[3]The Dodd-Walls Centre for Photonic and Quantum Technologies, New Zealand
[4]Chimie ParisTech, PSL University, CNRS, Institut de Recherche de Chimie Paris, 75005 Paris, France

(Received 5 September 2018; revised manuscript received 1 November 2018; published 31 July 2019)

We show that crystal-field calculations for C_1 point-group symmetry are possible, and that such calculations can be performed with sufficient accuracy to have substantial utility for rare-earth based quantum information applications. In particular, we perform crystal-field fitting for a C_1-symmetry site in $^{167}Er^{3+}:Y_2SiO_5$. The calculation simultaneously includes site-selective spectroscopic data up to 20 000 cm^{-1}, rotational Zeeman data, and ground- and excited-state hyperfine structure determined from high-resolution Raman-heterodyne spectroscopy on the 1.5 μm telecom transition. We achieve an agreement of better than 50 MHz for assigned hyperfine transitions. The success of this analysis opens the possibility of systematically evaluating the coherence properties, as well as transition energies and intensities, of any rare-earth ion doped into Y_2SiO_5.

DOI: 10.1103/PhysRevLett.123.057401

Over the last decade, substantial progress has been made towards realizing practical quantum information processing hardware using solid-state rare-earth ion based materials. Key areas of advancement have been optical quantum memories [1–10], quantum-gate implementations [11,12], single photon sources [13–15], and microwave-to-optical photon modulators [16]. To date, one of the host materials of choice for these applications has been yttrium orthosilicate (Y_2SiO_5). The reason for this is twofold: first, yttrium has a very small nuclear magnetic moment, while isotopes of Si and O with nonzero nuclear spin have very low natural abundances. At cryogenic temperatures, nuclear spin flips are the primary source of decoherence in rare-earth ion doped materials, resulting in Y_2SiO_5 based systems having outstanding coherence properties. The second reason is that the rare-earth substitutional site in Y_2SiO_5 has a C_1 point-group symmetry; this leads to highly admixed wave functions enabling efficient and diverse optical pumping schemes [11,17,18].

The formulation of accurate models for the hyperfine structure of C_1 point-group symmetry sites is highly nontrivial; however, they are an invaluable tool for a number of practical applications. For example, the availability of the spin Hamiltonian for $^{151}Eu^{3+}:Y_2SiO_5$ allowed for a computational search for magnetic field orientations exhibiting a near-zero gradient with respect to hyperfine energy levels. This is the basis of the zero-first-order-Zeeman (ZEFOZ) technique, which was essential to the experimental demonstration of a coherence time of six hours [5]. However, spin Hamiltonian models are restricted to specific electronic levels of a single ion-host combination. This results in considerable practical challenges, especially for the structure of the excited-state electronic levels, which can often only be probed using experiments that conflate excited and ground state splittings. In this Letter, we avoid the shortcomings of spin Hamiltonians by developing a method to fit a crystal-field Hamiltonian for erbium doped Y_2SiO_5.

Crystal-field methods have been essential to the development of rare-earth optical applications, such as phosphors and lasers [19–21]. However, the lack of symmetry (i.e., C_1 symmetry) of rare-earth substitutional sites in Y_2SiO_5 hindered the application of crystal-field modeling to this material, despite its ubiquity as a host in quantum-information applications. Previous work on C_1 symmetry sites was based on *ab initio* calculations [22,23] or used a higher-symmetry approximation to reduce the number of parameters [24,25]. These approaches are not accurate enough to model the complex magnetic and hyperfine structure that we consider in this Letter. The key advantage of a crystal-field model over the spin Hamiltonian approach is that it is not restricted to a specific electronic level but predicts the magnetic and hyperfine structure of the complete $4f$ configuration. This greatly increases the predictive power, aids the analysis of excited states, and also enables fitting to a much wider range of experimental data. Further, crystal-field modeling enables the rigorous calculation of radiative transition rates [21,26].

The predictive power of crystal-field models extends considerably beyond an individual rare-earth ion. For a fixed host crystal, there exist well established parameter trends across the rare-earth series [27]. Consequently,

parameters describing a specific rare-earth dopant can be extrapolated to previously unstudied rare-earth dopants in the same host. Moreover, the availability of complete $4f^{11}$ wave functions enables several novel applications, such as studying ZEFOZ points in a large magnetic field, a regime in which the spin Hamiltonian approach breaks down. A recent demonstration of coherence times exceeding one second in $^{167}Er^{3+}:Y_2SiO_5$ using a 7 T magnetic field makes this particularly relevant [7], since, if such an approach were to be combined with the ZEFOZ technique, an accurate model at large field would be imperative.

In this Letter, we report a phenomenological crystal-field fit for one of the C_1 symmetry sites of $^{167}Er^{3+}:Y_2SiO_5$. Physical properties, such as a transitions in the 1.5 μm telecommunications band and an optical homogeneous linewidth of 50 Hz [28] make this one of the most promising materials for rare-earth based quantum information applications. Despite extensive past characterization [22,29–35], an accurate model of the excited state hyperfine structure remains an outstanding problem. This material is, therefore, an important test case for crystal-field fitting to substitutional sites without symmetry. To achieve a unique fit, both site-selective optical as well as Zeeman and hyperfine data were required [36], which were available from the literature [22,34,35]. This was complemented with targeted Raman-heterodyne measurements to obtain high-precision hyperfine splittings of the ground and $^4I_{13/2}Y_1$ excited states.

Y_2SiO_5 is a monoclinic crystal with C_{2h}^6 space group symmetry. The yttrium ions occupy two crystallographically distinct sites, each with C_1 point-group symmetry, referred to as site 1 and site 2 [37]. Because of the wavelength tuning range of our laser, this work is focused on site 1. Y_2SiO_5 has three perpendicular optical-extinction axes: the crystallographic b axis, and two mutually perpendicular axes labeled D_1 and D_2. We follow the convention of identifying these axes as z, x, and y, respectively [34].

The complete Hamiltonian appropriate for modeling the $4f^n$ configuration reads

$$H = H_{\mathrm{FI}} + H_{\mathrm{CF}} + H_Z + H_{\mathrm{HF}} + H_Q. \tag{1}$$

The terms in the above equation represent the following interactions: the free-ion (FI) contribution, the crystal-field (CF) interaction, the Zeeman term, the nuclear magnetic dipole hyperfine (HF) interaction, and the nuclear quadrupole interaction. We use the usual free-ion Hamiltonian with the following parameters: E_0 accounting for a constant configurational shift, F^k, the Slater parameters characterizing aspherical electrostatic repulsion, and ζ, the spin-orbit coupling constant. Furthermore, we also include terms that parametrize two- and three-body interactions as well as higher-order spin-dependent effects; for a more detailed description, the reader is referred to the review by Liu [38]. The most general crystal-field Hamiltonian has the form

$$H_{\mathrm{CF}} = \sum_{k,q} B_q^k C_q^{(k)}, \tag{2}$$

for $k = 2, 4, 6$ and $q = -k \cdots k$. The B_q^k parameters are the crystal-field expansion coefficients, and $C_q^{(k)}$ are spherical tensor operators using Wybourne's normalization [39]. We write nonaxial ($q \neq 0$) B_q^k parameters as complex numbers. In this convention, the $\pm q$ parameters are related by $(B_q^k)^* = (-1)^q B_{-q}^k$ [40,41]. For the remaining terms in Eq. (1) we note that H_{HF} and H_Q, respectively, contain coupling constants A and Q that must be determined from experiment, while H_Z has no free parameters. For a detailed description of these terms, and the evaluation of their matrix elements, the reader is referred to Refs. [24,42].

High precision magnetic and hyperfine interactions are generally expressed using the spin Hamiltonian (SH) formalism [43]. For a Kramers ion with nonzero nuclear spin, this Hamiltonian has the form [44]

$$\mathcal{H} = \beta_e \boldsymbol{B}\cdot\boldsymbol{g}\cdot\boldsymbol{S} + \boldsymbol{I}\cdot\boldsymbol{A}\cdot\boldsymbol{S} + \boldsymbol{I}\cdot\boldsymbol{Q}\cdot\boldsymbol{I} - \beta_n g_n \boldsymbol{B}\cdot\boldsymbol{I}, \tag{3}$$

where β_e is the Bohr magneton, $\boldsymbol{B}$ is an external field vector, $\boldsymbol{g}$ is the g tensor, $\boldsymbol{A}$ is the hyperfine tensor, and $\boldsymbol{Q}$ is the electric-quadrupole tensor. Further, $\boldsymbol{S}$ and $\boldsymbol{I}$ are vectors of electronic and nuclear spin operators, respectively. β_n and g_n are the nuclear magneton and nuclear g factors, respectively. For the magnetic field values considered here, the nuclear Zeeman interaction is less than 2 MHz, and since the uncertainty of $\boldsymbol{A}$ and $\boldsymbol{Q}$ is $O(20\ \mathrm{MHz})$ [35] this interaction is neglected.

For the initial phase of our fitting, we use a projection from the crystal-field Hamiltonian to the spin Hamiltonian, so that we can fit to spin-Hamiltonian parameters. This projection has the form

$$A_{\mathrm{SH}} = V^\dagger A V, \tag{4}$$

for operator A and spin Hamiltonian effective operator A_{SH}. Here, V are the eigenvectors one obtains by diagonalizing $H_{\mathrm{FI}} + H_{\mathrm{CF}}$, which can be interpreted as the zero order contribution to the spin Hamiltonian.

For C_1 symmetry, this projection has some subtleties; specifically, there is a phase freedom in the matrix elements of $\boldsymbol{S}$ and $\boldsymbol{I}$ in Eq. (3). This phase freedom does not affect the eigenvalue spectrum of the spin Hamiltonian; nevertheless, a specific orientation is required in order for the parameter tensors to be symmetric. When one determines spin Hamiltonian parameter matrices from experimental data, this issue is avoided, for by choosing symmetric parameter matrices during the fitting, one implicitly fixes the phase to an appropriate value. However, when one performs the projection (4), the value of this phase does not necessarily correspond to a symmetric parameter tensor. We mitigate this by employing a singular-value decomposition to transform the spin Hamiltonian tensors to a basis in which they

are always symmetric. For our calculations, this phase was identically zero for matrix elements of $\boldsymbol{I}$, and therefore, we only discuss matrix elements of $\boldsymbol{S}$. We consider, as an example, the Zeeman interaction term. Given the unitary matrices $\boldsymbol{U}$ and $\boldsymbol{V}$ and the diagonal matrix $\boldsymbol{\Sigma}$, the singular value decomposition of $\boldsymbol{g}$ takes the form

$$\boldsymbol{g} = \boldsymbol{U}\boldsymbol{\Sigma}\boldsymbol{V}^{\dagger}. \tag{5}$$

Consequently, $\boldsymbol{U}^{\dagger}\boldsymbol{g}\boldsymbol{V}$ is diagonal, and performing a similarity transformation with the unitary matrix $\boldsymbol{U}$, we obtain the symmetric tensor

$$\boldsymbol{U}\boldsymbol{U}^{\dagger}\boldsymbol{g}\boldsymbol{V}\boldsymbol{U}^{\dagger} = \boldsymbol{g}\boldsymbol{V}\boldsymbol{U}^{\dagger}. \tag{6}$$

Thus, we can define a transformed set of electronic spin operators $\boldsymbol{S}' = \boldsymbol{R}\boldsymbol{S}$ with $\boldsymbol{R} = \boldsymbol{V}\boldsymbol{U}^{\dagger}$, leading to an SU(2) transformed spin Hamiltonian term of the form $\boldsymbol{B}\cdot\boldsymbol{g}'\cdot\boldsymbol{S}'$, with $\boldsymbol{g}' = \boldsymbol{g}\boldsymbol{V}\boldsymbol{U}^{\dagger}$ symmetric. An analogous procedure can be applied to the nuclear dipole interaction term $\boldsymbol{I}\cdot\boldsymbol{A}\cdot\boldsymbol{S}$.

The crystal-field fit was performed in two phases: an initial coarse fitting which excluded high-resolution Raman-heterodyne data, and a second polishing phase where hyperfine transition data were iteratively added. The initial fitting employed site-selective excitation and fluorescence data from Doualan *et al.* [22], while simultaneously including the g tensor of the ${}^4\mathrm{I}_{13/2}Y_1$ level reported by Sun *et al.* [34], as well as the complete ground-state spin Hamiltonian reported by Chen *et al.* [35]. The site-selective data was, as usual in crystal-field calculations, directly fit to the eigenvalues of Eq. (1). In order to simultaneously fit to spin Hamiltonian data, the projection (4) was utilized to obtain a theoretical set of parameter matrices which could be fitted to their experimental counterparts.

This procedure yielded a set of parameters of sufficient accuracy to identify several ${}^4\mathrm{I}_{13/2}$ hyperfine transitions in our Raman-heterodyne data and, thus, complete the coarse step of the fitting. In order to perform the polishing stage, the projection (4) was abandoned, and instead, the Hamiltonian (1) was evaluated for a range of magnetic field values to directly obtain eigenvalues describing both the hyperfine structure as well as the site-selective data. This has the advantage that Raman-heterodyne data could be added step-by-step as transitions were identified. In order to ease the computational burden, the calculations of hyperfine states were performed using a truncated basis using the intermediate-coupling method described by Carnall *et al.* [27]. All software used to perform these calculations is available from [45].

Raman-heterodyne spectroscopy was performed for two separate frequency regions. Between 0 and 100 MHz, we use a radio frequency coil, and between 600 and 1200 MHz, a tunable aluminium single-loop single-gap resonator was used. Samples were cooled using a home built cryostat (containing a Cryomech PT405 pulsetube cooler) with an HTS-100 Ltd. superconducting vector magnet to provide an arbitrarily-oriented magnetic field. The light source was a Koheras AdjustiK E15 fiber laser, operating at 1536.48 nm on resonance with the ${}^4\mathrm{I}_{15/2} \rightarrow {}^4\mathrm{I}_{13/2}$ transition of site 1. The sample was an isotopically purified ${}^{167}\mathrm{Er}^{3+}:\mathrm{Y}_2\mathrm{SiO}_5$ crystal (Scientific Materials Inc.) with ${}^{167}\mathrm{Er}^{3+}$ substituted for Y^{3+} ions at a 50 ppm level. For a more detailed description of Raman-heterodyne spectroscopy, as well as the experimental setup and methods, the reader is referred to Ref. [46], which employed the same Raman-heterodyne setup to identify transitions with long spin-coherence times.

Figure 1 shows the hyperfine transitions of both the ground and excited states with resonances in the 600–1200 MHz region with respect to a small change in magnetic field along the D_2 axis. These measurements are for site 1 of ${}^{167}\mathrm{Er}^{3+}:\mathrm{Y}_2\mathrm{SiO}_5$. Most transitions were studied in further detail using higher resolution scans over restricted subfrequencies to provide detailed curvatures for comparison with our model. Furthermore, low frequency data at 85 MHz included curvatures with respect to an external field along the D_1, D_2, and b axes. The maximum deviation of any Raman-heterodyne transition that we directly fit to was 15 MHz. For a few transitions the assignments remained ambiguous due to the closely spaced spectral lines. The maximum difference between an observed transition and its theoretical prediction was 50 MHz, approximately 1% of the span of the hyperfine levels. We note that, using our final transition assignments, the coarse fitting predicted ${}^4\mathrm{I}_{13/2}Y_1$ transition frequencies to within ~200 MHz of their measured values. Thus, while using only ground-state hyperfine data enabled the

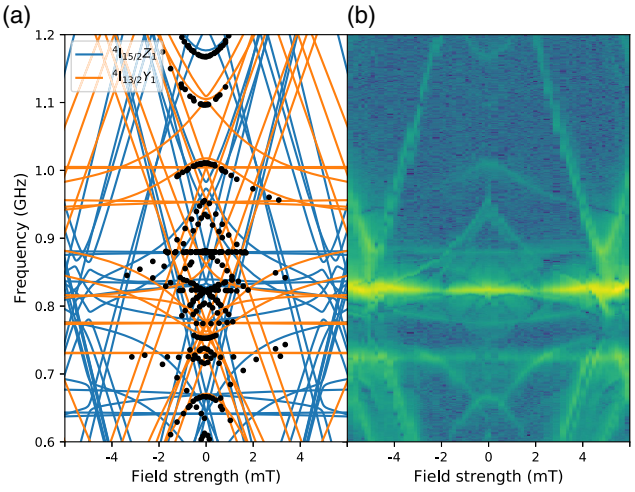

FIG. 1. (a) Raman-heterodyne data (black markers) showing hyperfine transitions of the first levels of both the ${}^4\mathrm{I}_{15/2}$ and ${}^4\mathrm{I}_{13/2}$ multiplets of site 1 in $\mathrm{Er}^{3+}:\mathrm{Y}_2\mathrm{SiO}_5$, superimposed with predictions from our crystal-field model. The magnetic field was varied in the direction of the D_2 axis. (b) A Raman-heterodyne scan of this region; the color map uses a linear scale of arbitrary intensity with yellow or green indicating a resonance condition.

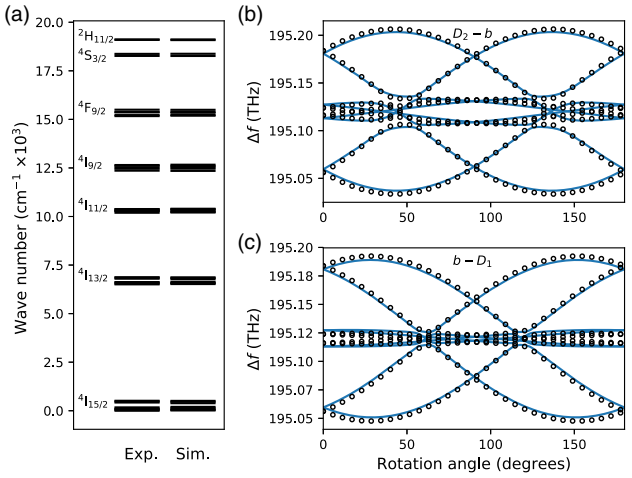

FIG. 2. (a) Experimental and simulated crystal-field level splittings up to $^2H_{11/2}$ for site 1 of $Er^{3+}:Y_2SiO_5$; experimental values are from Doualan *et al.* [22]. (b) and (c) Rotation patterns for optical transitions between $^4I_{15/2}Z_1$ and $^4I_{13/2}Y_1$. Circles denote the predictions using g-tensor data from Sun *et al.* [34], while the solid lines correspond to our crystal-field model. The magnetic field magnitude used was 0.484 T, and the labels $D_2 - b$ and $b - D_1$ indicate the rotation planes using the standard orthogonal axes notation for Y_2SiO_5.

prediction of excited-state hyperfine transitions with reasonable accuracy, further fitting was required to obtain an optimal model.

Given that similar ground-state data is available for crystallographic site 2 of $^{167}Er^{3+}:Y_2SiO_5$ [35], a model with comparable accuracy to the coarse fitting presented here should, in principle, be possible; however, such an analysis is beyond the scope of this work.

In Fig. 2, we show the spread of electronic data for energies up to 20 000 cm^{-1} and include detailed magnetic rotation data of the transition between the lowest $^4I_{13/2}$ level and the ground state, with splittings on the order of 200 GHz [34]. In Table I, we present the complete set of parameters determined from our calculation. We note that, since the Zeeman and hyperfine splittings are much smaller in magnitude and are determined with higher accuracy than the crystal-field level energies, they were given more weight in the parameter fit.

The parameter uncertainties shown in Tab. I were estimated using the Markov chain Monte Carlo technique. In the Supplemental Material [47], which includes Refs. [48–51], we provide a more detailed description of the fitting procedure. We also include all predicted crystal-field level energies up to $^2H_{11/2}$ for a direct comparison with experimental values from Ref. [22]. Furthermore, the Raman-heterodyne data for the 0–120 MHz frequency window is presented and plotted together with the corresponding theoretical transition energies. The Zeeman and hyperfine tensors for both the Z_1 and Y_1 electronic levels are tabulated in the Supplemental Material [47].

TABLE I. Fitted values for the free-ion and crystal-field parameters for site 1 of $Er^{3+}:Y_2SiO_5$. The Judd and Tree's parameters, which are not included here, were fixed to the values obtained for $Er^{3+}:LaF_3$ by Carnall *et al.* [27].

Parameter	Fitted value (cm^{-1})	Uncertainty (cm^{-1})
E_0	35 503.5	19.8
ζ	2362.9	1.8
F^2	96 029.6	183.7
F^4	67 670.6	223.2
F^6	53 167.1	263.7
B_0^2	−149.8	5.4
B_1^2	420.6 + 396.0i	3.1 + 1.3i
B_2^2	−228.5 + 27.6i	1.8 + 3.4i
B_0^4	1131.2	30.4
B_1^4	985.7 + 34.2i	7.0 + 6.7i
B_2^4	296.8 + 145.0i	9.0 + 4.1i
B_3^4	−402.3 − 381.7i	9.7 + 8.9i
B_4^4	−282.3 + 1114.3i	13.4 + 12.0i
B_0^6	−263.2	3.1
B_1^6	111.9 + 222.9i	1.5 + 3.9i
B_2^6	124.7 + 195.9i	2.1 + 3.8i
B_3^6	−97.9 + 139.7i	5.1 + 9.7i
B_4^6	−93.7 − 145.0i	4.1 + 3.0i
B_5^6	13.9 + 109.5i	2.0 + 6.1i
B_6^6	3.0 − 108.6i	8.6 + 2.4i
A	0.005 466	0.000 003
Q	0.0716	0.0003

In the crystal-field analysis, 34 parameters (five free-ion parameters, 27 crystal-field parameters, and two hyperfine parameters) are fitted to 95 data points (enumerated in the Supplemental Material [47]). By comparison, two separate spin Hamiltonians, requiring, in total, 34 parameters, would be required for a conventional analysis of the two states. The advantage of our approach is that a fit to the ground state hyperfine data yields a prediction of the excited state hyperfine structure. This enables simultaneous fitting to both ground and excited state data to obtain a high-precision $4f^{11}$ Hamiltonian.

In conclusion, we have demonstrated a crystal-field fit for a rare-earth substitutional site with no symmetry. This enabled us to accurately characterize the hyperfine structure of the ground state and all excited state levels of $^{167}Er^{3+}:Y_2SiO_5$, allowing modeling of optical pumping schemes via the 1.5 μm (or other) transitions, as well as high-field ZEFOZ applications. With suitable scaling, the crystal-field parameters are also applicable to other ions in Y_2SiO_5, opening the possibility of identifying promising transitions prior to extensive experimental investigation.

The authors wish to acknowledge the use of New Zealand eScience Infrastructure (NeSI) high performance computing facilities as part of this research and financial

support from the Marsden Fund of the Royal Society of New Zealand through Contract No. UOO1520. S. P. H. acknowledges financial support in the form of a Canterbury Scholarship by the University of Canterbury. P. G. would like to thank the University of Canterbury for support in the form of an Erskine Fellowship.

*Corresponding author.
sebastian.horvath@gmail.com
†Corresponding author.
mike.reid@canterbury.ac.nz

[1] H. de Riedmatten, M. Afzelius, M. U. Staudt, C. Simon, and N. Gisin, Nature (London) **456**, 773 (2008).
[2] M. P. Hedges, J. J. Longdell, Y. Li, and M. J. Sellars, Nature (London) **465**, 1052 (2010).
[3] P. Jobez, C. Laplane, N. Timoney, N. Gisin, A. Ferrier, P. Goldner, and M. Afzelius, Phys. Rev. Lett. **114**, 230502 (2015).
[4] M. Gündoğan, P. M. Ledingham, K. Kutluer, M. Mazzera, and H. de Riedmatten, Phys. Rev. Lett. **114**, 230501 (2015).
[5] M. Zhong, M. P. Hedges, R. L. Ahlefeldt, J. G. Bartholomew, S. E. Beavan, S. M. Wittig, J. J. Longdell, and M. J. Sellars, Nature (London) **517**, 177 (2015).
[6] T. Zhong, J. M. Kindem, J. G. Bartholomew, J. Rochman, I. Craiciu, E. Miyazono, M. Bettinelli, E. Cavalli, V. Verma, S. W. Nam, F. Marsili, M. D. Shaw, A. D. Beyer, and A. Faraon, Science **357**, 1392 (2017).
[7] M. Rančić, M. P. Hedges, R. L. Ahlefeldt, and M. J. Sellars, Nat. Phys. **14**, 50 (2018).
[8] B. Lauritzen, J. Minář, H. de Riedmatten, M. Afzelius, N. Sangouard, C. Simon, and N. Gisin, Phys. Rev. Lett. **104**, 080502 (2010).
[9] C. Laplane, P. Jobez, J. Etesse, N. Gisin, and M. Afzelius, Phys. Rev. Lett. **118**, 210501 (2017).
[10] A. Seri, A. Lenhard, D. Rieländer, M. Gündoğan, P. M. Ledingham, M. Mazzera, and H. de Riedmatten, Phys. Rev. X **7**, 021028 (2017).
[11] J. J. Longdell and M. J. Sellars, Phys. Rev. A **69**, 032307 (2004).
[12] L. Rippe, B. Julsgaard, A. Walther, Y. Ying, and S. Kröll, Phys. Rev. A **77**, 022307 (2008).
[13] R. Kolesov, K. Xia, R. Reuter, R. Stöhr, A. Zappe, J. Meijer, P. R. Hemmer, and J. Wrachtrup, Nat. Commun. **3**, 1029 (2012).
[14] T. Utikal, E. Eichhammer, L. Petersen, A. Renn, S. Götzinger, and V. Sandoghdar, Nat. Commun. **5**, 3627 (2014).
[15] A. M. Dibos, M. Raha, C. M. Phenicie, and J. D. Thompson, Phys. Rev. Lett. **120**, 243601 (2018).
[16] X. Fernandez-Gonzalvo, Y.-H. Chen, C. Yin, S. Rogge, and J. J. Longdell, Phys. Rev. A **92**, 062313 (2015).
[17] L. Rippe, M. Nilsson, S. Kröll, R. Klieber, and D. Suter, Phys. Rev. A **71**, 062328 (2005).
[18] B. Lauritzen, S. R. Hastings-Simon, H. de Riedmatten, M. Afzelius, and N. Gisin, Phys. Rev. A **78**, 043402 (2008).
[19] W. Krupke, IEEE J. Quantum Electron. **7**, 153 (1971).
[20] B. R. Judd, in *Handbook on the Physics and Chemistry of Rare Earths*, Two-Hundred-Year Impact of Rare Earths on Science Vol. 11 (Elsevier, New York, 1988), pp. 81–195.
[21] C. Görller-Walrand and K. Binnemans, in *Handbook on the Physics and Chemistry of Rare Earths* (Elsevier, New York, 1998), Vol. 25 pp. 101–264.
[22] J. L. Doualan, C. Labbe, P. L. Boulanger, J. Margerie, R. Moncorge, and H. Timonen, J. Phys. Condens. Matter **7**, 5111 (1995).
[23] J. Wen, C.-K. Duan, L. Ning, Y. Huang, S. Zhan, J. Zhang, and M. Yin, J. Phys. Chem. A **118**, 4988 (2014).
[24] O. Guillot-Noël, Y. Le Du, F. Beaudoux, E. Antic-Fidancev, M. F. Reid, R. Marino, J. Lejay, A. Ferrier, and P. Goldner, J. Lumin. **130**, 1557 (2010).
[25] A. A. Sukhanov, R. F. Likerov, R. M. Eremina, I. V. Yatsyk, T. P. Gavrilova, V. F. Tarasov, Y. D. Zavartsev, and S. A. Kutovoi, J. Magn. Reson. **295**, 12 (2018).
[26] M. F. Reid, in *Spectroscopic Properties of Rare Earths in Optical Materials*, edited by G. Liu and B. Jacquier (Springer Science & Business Media, Berlin, 2006).
[27] W. T. Carnall, G. L. Goodman, K. Rajnak, and R. S. Rana, J. Chem. Phys. **90**, 3443 (1989).
[28] Y. Sun, C. W. Thiel, R. L. Cone, R. W. Equall, and R. L. Hutcheson, J. Lumin. **98**, 281 (2002).
[29] T. Böttger, C. W. Thiel, Y. Sun, and R. L. Cone, Phys. Rev. B **73**, 075101 (2006).
[30] T. Böttger, C. W. Thiel, R. L. Cone, and Y. Sun, Phys. Rev. B **77**, 155125 (2008).
[31] E. Baldit, K. Bencheikh, P. Monnier, S. Briaudeau, J. A. Levenson, V. Crozatier, I. Lorgeré, F. Bretenaker, J. L. Le Gouët, O. Guillot-Noël, and P. Goldner, Phys. Rev. B **81**, 144303 (2010).
[32] B. Lauritzen, S. R. Hastings-Simon, H. de Riedmatten, M. Afzelius, and N. Gisin, Phys. Rev. A **78**, 043402 (2008).
[33] R. P. Budoyo, K. Kakuyanagi, H. Toida, Y. Matsuzaki, W. J. Munro, H. Yamaguchi, and S. Saito, Phys. Rev. Mater. **2**, 011403 (2018).
[34] Y. Sun, T. Böttger, C. W. Thiel, and R. L. Cone, Phys. Rev. B **77**, 085124 (2008).
[35] Y.-H. Chen, X. Fernandez-Gonzalvo, S. P. Horvath, J. V. Rakonjac, and J. J. Longdell, Phys. Rev. B **97**, 024419 (2018).
[36] S. P. Horvath, J.-P. R. Wells, M. F. Reid, M. Yamaga, and M. Honda, J. Phys. Condens. Matter **31**, 015501 (2019).
[37] B. Maksimov, V. Ilyukhin, Y. A. Kharitonov, and N. Belov, Sov. Phys. Crystallogr. **15**, 806 (1971).
[38] G. Liu, in *Spectroscopic Properties of Rare Earths in Optical Materials*, edited by G. Liu and B. Jacquier (Springer Science & Business Media, Berlin, 2006).
[39] B. G. Wybourne, *Spectroscopic Properties of Rare Earths* (Interscience Publishers, New York, 1965).
[40] D. J. Newman and B. Ng, Rep. Prog. Phys. **52**, 699 (1989).
[41] D. J. Newman and B. Ng, *Crystal Field Handbook* (Cambridge University Press, Cambridge, England, 2007).
[42] D. P. McLeod and M. F. Reid, J. Alloys Compd. **250**, 302 (1997).
[43] R. M. Macfarlane and R. M. Shelby, in *Spectroscopy of Solids Containing Rare Earth Ions*, edited by A. A. Kaplyanskii and R. M. Macfarlane (North-Holland, Amsterdam, 1987).

[44] A. Abragam and B. Bleaney, *Electron Paramagnetic Resonance of Transition Ions* (Clarendon Press, Oxford, 1970).
[45] S. P. Horvath, The pycf crystal-field theory package, https://bitbucket.org/sebastianhorvath/pycf.
[46] J. V. Rakonjac, Y.-H. Chen, S. P. Horvath, and J. J. Longdell, arXiv:1802.03862.
[47] See Supplemental Material at http://link.aps.org/supplemental/10.1103/PhysRevLett.123.057401 for $^4I_{13/2}Y_1$ spin Hamiltonian parameters, crystal-field level predictions up to the $^2H_{11/2}$ multiplet, and a detailed description of the crystal-field fitting procedure.
[48] D. J. Wales and J. P. K. Doye, J. Phys. Chem. A **101**, 5111 (1997).
[49] T. H. Rowan, Ph.D. thesis, University of Texas at Austin, 1990.
[50] S. G. Johnson, The NLopt nonlinear-optimization package, http://ab-initio.mit.edu/nlopt.
[51] R. C. Aster, B. Borchers, and C. H. Thurber, *Parameter Estimation and Inverse Problems* (Academic Press, New York, 2011), Vol. 90.